MECSOL 2019 - Proceedings of the 7th International Symposium on Solid Mechanics,
V. Tita, A. Ferreira, M.L. Ribeiro, A. Vieira and A.T. Beck (Editors), ABCM, Sao Carlos, SP, Brazil, April 15th to 17th, 2019

Numerical Evaluation of an Onboard Composite Hollow Shaft

Paulo Costa Porto de Figueiredo Barbosa, Marcelo Samora Sousa Jr, Vergílio Torezan Silingardi Del-Claro, Aldemir Ap Cavalini Jr, Valder Steffen Jr

LMEst - Structural Mechanics Laboratory, Federal University of Uberlândia, School of Mechanical Engineering, Av. João Naves de Ávila, 2121, Uberlândia, MG, 38408-196, Brazil.

Abstract: Composite materials have been extensively used in engineering applications over the past few decades, presenting interesting mechanical characteristics over the standard metallic materials. In many rotating systems, the dynamics of the shaft can be improved when composite materials are applied due to their smaller inertias, low weight, and high strength. In this sense, composite shafts demonstrated to be interesting for rotating machines on onboard applications since composite shafts allow for mechanical properties manipulation by adjusting fiber and matrix composition, layer orientation, layer thickness, and other geometric properties. Simplified theories are commonly considered for the modeling of composite shafts. Most theories aim at providing sufficiently accurate vibration responses of the system with low computational cost. In this contribution, the Simplified Homogenized Beam Theory (SHBT) was explored, associated with the additional considerations for the onboard rotordynamics representation. A finite element model was simulated for different operating conditions and its vibration responses were presented.

Keywords: composite hollow shaft, onboard rotor, finite element model, SHBT.

INTRODUCTION

The use of composite materials has been growing over the years, mainly in naval, aeronautical, and automotive industries, due to the range of possibilities in obtaining suitable characteristics for different situations. Rotordynamics is one of the areas with interest in the use of composite shafts since they are a viable solution to overcome the limitations inherent to metal shafts (Silveira, 2001). For systems operating under subcritical conditions (rigid rotors), the goal is to decrease weight and maximize the torque transmission. The low weight of composite shafts allows for the faster run-up and run-down procedures of the machines when compared with conventional metallic shafts (Brush, 1999). However, in supercritical operations (flexible rotors) the vibration responses associated with the shaft bending, dynamic stress, stability, and fatigue should be carefully evaluated (Gupta, 2015).

In composite shafts, it is possible to change stiffness and damping properties by manipulating some characteristics such as adjusting fiber and matrix composition, fiber orientation, number of layers, stacking sequence, and layer thickness. This allows for the critical velocities to be conveniently changed according to the use of the rotor. Additionally, it is possible to attenuate the vibration amplitudes when the system undergoes critical speeds (Silveira, 2001).

The internal damping can change the dynamic behavior of composite shafts, reducing their vibration amplitudes at critical speeds. However, instability can be achieved under certain conditions (Silveira, 2001). In rotors with metallic shafts, the influence of the internal damping can be omitted in most cases. Nevertheless, in composite shafts, it can be up to twice as large as on a conventional shaft (Wettergren and Olsson, 1996). In this context, the characterization of the internal damping is important to design rotating machines with composite shafts aiming to establish a safe operating condition.

Another application for composites is on onboard situations, in which the bearings holding the rotor will be submitted to external forces and excitations. Machines on high-sea offshore platforms, vehicles in general, and earthquake-resistant machinery are some examples of onboard rotors. Regarding the aeronautical applications, the aircraft engine is considered a typical onboard rotor which has its dynamic behavior influenced by external base excitations. A mathematical model able to faithfully represent the dynamic behavior of onboard rotors is obtained by considering various subsystems, as follows: firstly, the subsystems that can be defined by its geometry, such as the disks and couplings. Later, the subsystems that are dependent on the frequency and/or lateral displacements and velocities of the shaft, such as rolling or hydrodynamic bearings, the gyroscopic effect, and the efforts applied in the system through its base. Finally, the shaft, typically modeled by using the FE method and, when required, adopting hypotheses aiming at representing the dynamic behavior of composite materials.

Simplifying hypotheses are commonly used to model composite shafts, allowing for the dynamic behavior of the system to be sufficiently accurately represented. Various finite element formulations based on the homogeneous beam

theory and shell theory have been proposed for the analysis of composite shafts. In this study, the Simplified Homogenized Beam Theory (SHBT) was used, as proposed by Sino (2007). Proper considerations were made, regarding the dynamic effects coming from the onboard dynamics. The numerical results are presented in time and frequency domains, demonstrating the ability of the SHBT model to represent the dynamic behavior of onboard composite shaft rotors.

ROTOR MODEL

Figure 1 shows the representation used for an onboard rotor in which three reference axis systems are used (Duchemin et al., 2006).

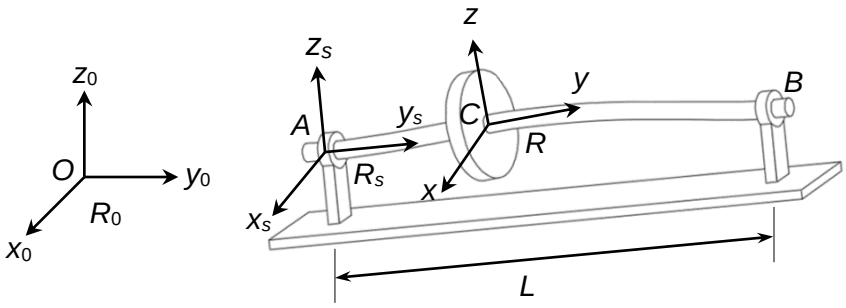

Figure 1 – Onboard rotor schematic representation (Duchemin 2003)

The movement of referential R_s relative to the R coordinate system is described by ψ, θ, and ϕ angles. R orientation is obtained from a ψ rotation around z_s, leading to an intermediate referential R_1 (x_1, y_1, z_1); a θ rotation around x_1 is afterward performed, resulting in the referential R_2 (x_2, y_2, z_2); and finally, a ϕ rotation around y is performed. After further considerations, Eq. (1) presents the differential equation that represents the dynamic behavior of a flexible onboard rotor operating in a steady state condition (Lalanne and Ferraris, 1998).

$$\boldsymbol{M}\ddot{\delta} + \left[\boldsymbol{D} + \boldsymbol{D}^* + \Omega \boldsymbol{D}_g\right]\dot{\delta} + [\boldsymbol{K} + \boldsymbol{K}^*]\delta = \boldsymbol{W} + \boldsymbol{F}_u + \boldsymbol{F}_u{}^* \tag{1}$$

where $\boldsymbol{M}$ is the mass matrix, $\boldsymbol{D}$ is the damping matrix associated with the bearings, $\boldsymbol{D}_g$ represents the gyroscopic effect, and $\boldsymbol{K}$ is the stiffness matrix. The vector δ represents the generalized displacements of the shaft (lateral displacements) and $\boldsymbol{W}$ is the rotation speed. $\boldsymbol{W}$ stands for the weight of the rotating parts and $\boldsymbol{F}_u$ represents the unbalance forces. The superscript * terms represent the additional terms due to the dynamic effects of the onboard consideration.

Considering the dissipative effects associated with composite materials (Sino, 2007), Eq. (1) is modified as follows:

$$\boldsymbol{M}\ddot{\delta} + \left[\boldsymbol{D} + \boldsymbol{D}^* + \Omega \boldsymbol{D}_g + \boldsymbol{D}_i\right]\dot{\delta} + [\boldsymbol{K} + \boldsymbol{K}^* + \Omega \boldsymbol{K}_i]\delta = \boldsymbol{W} + \boldsymbol{F}_u + \boldsymbol{F}_u{}^* \tag{2}$$

where $\boldsymbol{D}_i$ and $\boldsymbol{K}_i$ are the internal damping and the stiffness matrices, respectively, both associated with the composite material.

COMPOSITE HOLLOW SHAFT

The composite hollow shaft studied in this work is provided by Rock West Composites®. The shaft is manufactured by using special high-modulus pre-impregnated carbon fiber plies. Figure 2 illustrates the analyzed composite hollow shaft.

The analyzed composite material has twenty layers with the following stacking sequence: [0 0 0 0 90 90 45 -45 0 0 0 45 -45 90 90 0 0 0 0 0/90] (degrees). Table 1 summarizes the physical and geometric properties of the composite hollow shaft provided by Rock West Composites® and presented in Fig. 2.

Figure 2 – Composite hollow shaft used in the present contribution.

Table 1 – Physical and geometric properties of the composite hollow shaft.

Disks Properties	Value
Length [m]	0.907
Outer diameter [m]	0.018
Inner diameter [m]	0.0128
Density [kg/m³]	1667

Figure 3 shows a schematic representation regarding the directions of the fibers related to the Cartesian system, which follows the inertial directions defined for the analyzed rotor system (see the inertial directions defined in Fig. 1). In this case, 1, 2, and 3 are orthotropic axes associated with the fiber direction, the transversal direction to the fibers in the ply, and the perpendicular direction to the ply, respectively; φ is the angular direction of the fibers (Sino et al., 2008).

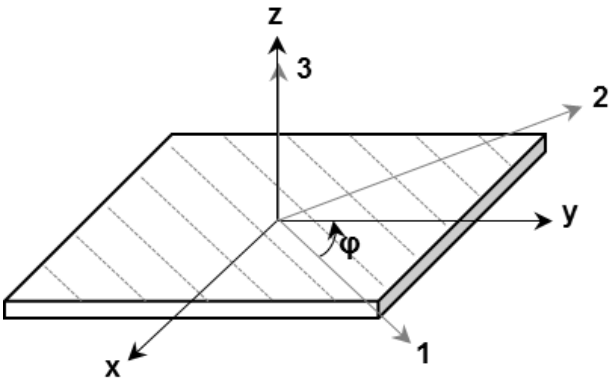

Figure 3 – Schematic representation regarding the directions of the fibers with respect to the Cartesian system.

The homogenized flexural stiffness *EI* of the composite hollow shaft is determined following the SHBT theory, as is given by Eq. (3).

$$EI = \sum_{p=1}^{N} E_y^p I^p$$
$$I^p = \frac{\pi}{4}(R_p^4 - R_{p-1}^4) \tag{3}$$

where I^p represents the inertia moment of area, R_{p-1} is the inner radius, and R_p is the outer radius; all of then associated with the ply *p*. The Young's modulus E_y^p of each ply is obtained by using Eq. (4).

$$E_y^p(\varphi) = \frac{1}{\frac{c^4}{E_l} + \frac{s^4}{E_t} + c^2 s^2 \left(\frac{1}{G_{lt}} - 2\frac{\upsilon_{lt}}{E_t} \right)} \tag{4}$$

where s and c stands for sin(φ) and cos(φ), respectively. E_l and E_t are the longitudinal and transversal Young's modulus associated with each ply p. The shear modulus is given by G_{lt} and υ_{lt} is the Poisson's ratio.

In order to determine the damping and stiffness matrices associated with the composite hollow shaft (i.e., $\mathbf{D}_i^q$ and $\mathbf{K}_i^q$, respectively; see Eq. (2)), the Kelvin-Voigt model (Sino, 2007) was used as shows Eq. (5).

$$\sigma = E\varepsilon + \eta E\dot{\varepsilon} \tag{5}$$

where σ and ε are the stress and strain fields, respectively, E is the Young's modulus, $\dot{\varepsilon} = d\varepsilon / dt$, and η is a dimensionless parameter. Note that the Kelvin-Voigt model comprises two parts, namely the linear stress-strain relationship given by the Hooke's law and the dissipation properties of the composite material.

The associated virtual work δW_s can be written as follows:

$$\delta W_s = \int_0^L \iint_S \left(E\varepsilon + \beta E\dot{\varepsilon} \right) \delta\varepsilon dS dy \tag{6}$$

in which the strain field is given by Eq. (7).

$$\varepsilon = -z\frac{\partial^2\left(u\cos\Omega t - w\sin\Omega t\right)}{\partial y^2} - x\frac{\partial^2\left(u\sin\Omega t + w\cos\Omega t\right)}{\partial y^2} \tag{7}$$

Applying Eq. (7) in Eq. (6) and considering $I = \int_s x^2\, dS = \int_s z^2\, dS$ and $\int_s xz\, dS = 0$, the virtual work δW_s is obtained, as shows Eq. (8).

$$\delta W_s = \beta EI \int_0^L \left(\frac{\partial^2 \dot{u}}{\partial y^2}\frac{\partial^2 \delta u}{\partial y^2} + \frac{\partial^2 \dot{w}}{\partial y^2}\frac{\partial^2 \delta w}{\partial y^2} - \Omega\frac{\partial^2 w}{\partial y^2}\frac{\partial^2 \delta u}{\partial y^2} + \Omega\frac{\partial^2 u}{\partial y^2}\frac{\partial^2 \delta w}{\partial y^2} \right) dy \tag{8}$$

The generalized forces are obtained applying the Equation (8) into $\delta W = -F_i^t \delta \mathbf{q}$. The resulting equations are applied on the Lagrange's equations (Lalanne and Ferraris, 1998), leading to the damping and stiffness matrices associated with the composite hollow shaft (finite element matrices $\boldsymbol{C}_i$ and $\boldsymbol{K}_i$, respectively; see Eq. (2)). The homogenized flexural stiffness EI derived from Eq. (3) and Eq. (4) is also used in Eq. (5) to obtain the strain energy U_s of the shaft and, consequently, the matrix $\boldsymbol{K}$ of Eq. (2).

MODEL UPDATING

The rotor test rig used in this work is shown in Fig. 4. It is composed of a horizontal composite hollow shaft, two aluminum disks, and two self-alignment ball bearings. Figure 5 shows the details of the components used in the considered test rig. Table 2 presents the physical and geometric properties of the disks. The components of the test rig are shown in Fig. 6.

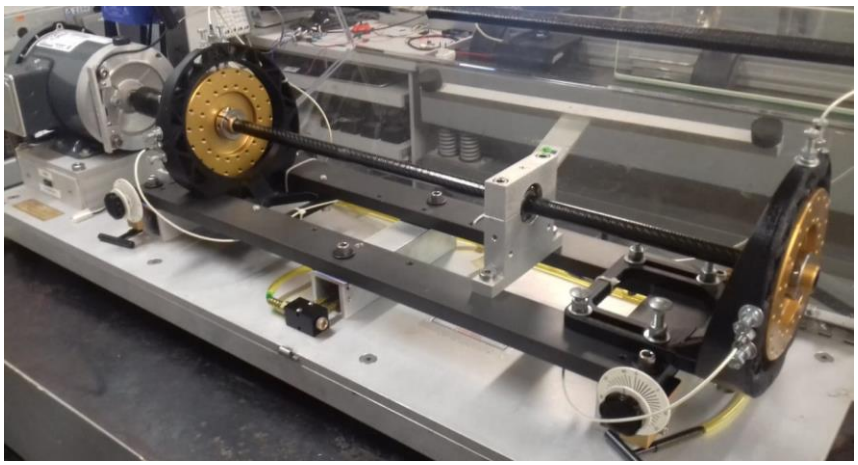

Figure 4 – Composite rotor test rig.

a) aluminum disks

b) aluminum coupling

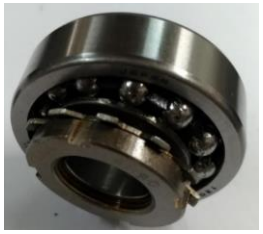

c) self-aligning ball bearings

Figure 5 – Test rig components.

Table 2 – Physical and geometric properties of the disks.

Disks Properties	Value
Thickness [m]	0.016
Outer diameter [m]	0.150
Inner diameter [m]	0.018
Density [kg/m³]	2700
Young's Modulus [Pa]	69×10^9

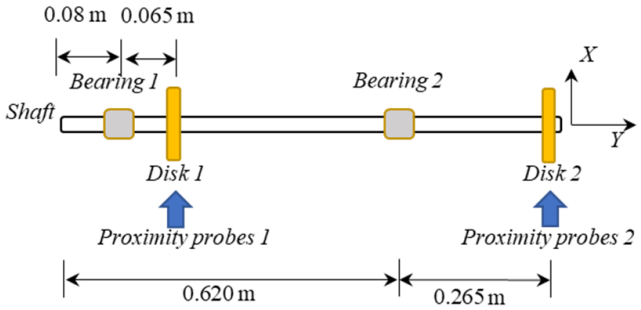

Figure 6 – Distribution of test rig components along the composite hollow shaft.

The physical properties of the shaft, the stiffness and damping coefficients of the bearings are presented in Tab. 3. These values were obtained by solving a typical inverse problem based on the numerical and experimental frequency response

Table 3 – Shaft parameters, bearing stiffness and damping coefficients, and unbalance masses.

Variable	Minimum Limit	Optimized Value	Maximum Limit
Young's modulus 0^0 [Pa]	$70x10^9$	$103.67x10^9$	$150x10^9$
Young's modulus 90^0 [Pa]	$70x10^9$	$127.05x10^9$	$150x10^9$
Young's modulus $0^0/90^0$ [Pa]	$20x10^9$	$47.49x10^9$	$80x10^9$
In-plane shear modulus [Pa]	$1x10^8$	$8.98x10^8$	$10x10^9$
In-plane shear modulus $0^0/90^0$ [Pa]	$1x10^8$	$3.04x10^9$	$10x10^9$
Major Poisson's ratio	0.05	0.3050	0.5
Major Poisson's ratio $0^0/90^0$	0.05	0.2802	0.5
η_1	$1x10^{-8}$	$2.67x10^{-7}$	$1x10^{-5}$
η_2	$1x10^{-8}$	$7.11x10^{-6}$	$1x10^{-5}$
η_3	$1x10^{-8}$	$6.58x10^{-6}$	$1x10^{-5}$
Bearing #1 - k_{xx} [N/m]	$1x10^3$	$866.77x10^3$	$1x10^7$
Bearing #1 - k_{zz} [N/m]	$1x10^3$	$182.37x10^3$	$1x10^7$
Bearing #1 - d_{xx} [Ns/m]	$1x10^2$	$64.58x10^3$	$1x10^6$
Bearing #1 - d_{zz} [Ns/m]	$1x10^2$	$6.86x10^3$	$1x10^6$
Bearing #2 - k_{xx} [N/m]	$1x10^3$	$10.005x10^3$	$1x10^7$
Bearing #2 - k_{zz} [N/m]	$1x10^3$	$10.004x10^3$	$1x10^7$
Bearing #2 - d_{xx} [Ns/m]	$1x10^2$	$9.06x10^3$	$1x10^6$
Bearing #2 - d_{zz} [Ns/m]	$1x10^2$	$1.02x10^3$	$1x10^6$
Mass unbalance - disk #1 [Kg.m]	$1x10^{-6}$	$3.44x10^{-3}$	$1x10^{-2}$
Phase - disk #1 [degrees]	0	340.51	360
Mass unbalance - disk #2 [Kg.m]	$1x10^{-6}$	$8.08x10^{-5}$	$1x10^{-2}$
Phase - disk #2 [degrees]	0	300.95	360

functions (FRFs). In this case, the differential evolution optimization approach was used (Storn and Price, 1995). It is worth mentioning that the shaft model was obtained by using the finite element method (33 Timoshenko beam elements), as presented by Lalanne and Ferraris (1998). Table 3 also shows the mass unbalance distribution along the considered test rig, which was determined by solving a similar inverse problem based on numerical and experimental vibration responses.

Figure 7 shows the numerical and experimental FRFs of the rotating machine. These FRFs were obtained by applying impacts along the *x* (Fig. 7a) and *z* (Fig. 7b) direction of the disk D_2 separately and the proximity probes installed along the corresponding directions. It can be observed that the updated finite element model is representative in the frequency bandwidth between 0 and 250 Hz, approximately. Figure 8 presents the numerical and experimental vibration responses of the rotating machine operating at 992 RPM. The time domain vibration responses were measured along the horizontal

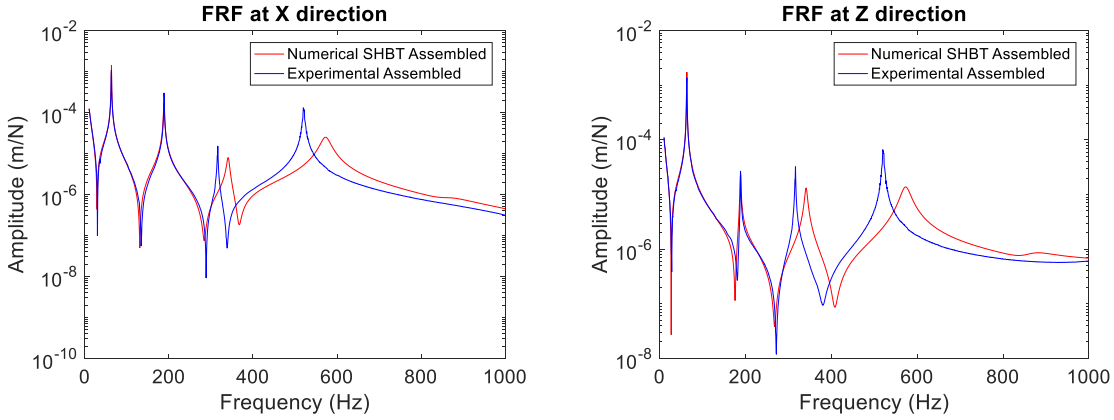

a) FRF at X direction **b) FRF at Z direction**

Figure 7 – Numerical and experimental FRFs of the rotating machine (---- experimental ---- numerical SHBT).

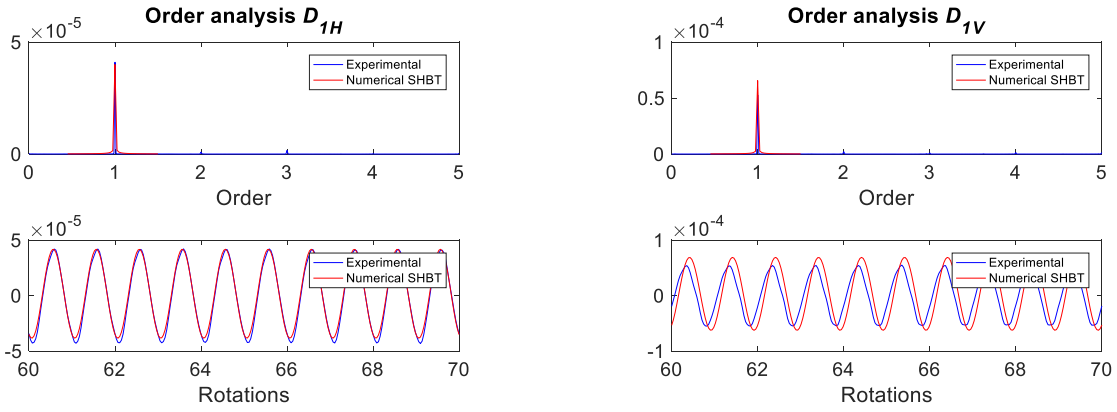

a) numerical and experimental vibration responses of disk D_1

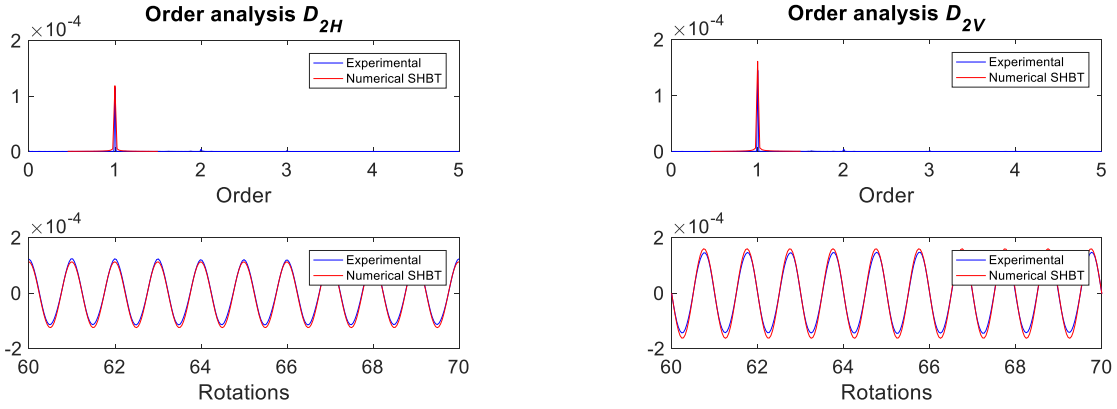

b) numerical and experimental vibration responses of disk D_2

Figure 8 – Numerical and experimental vibration responses of the rotating machine (---- experimental ---- numerical SHBT).

(*H*) and vertical (*V*) directions of the disk #1 (D_{1H} and D_{1V}, Fig. 8a) and disk #2 (D_{2H} and D_{2V}, Fig. 8a), see Fig. 4 and Fig. 6. Note that the numerical and experimental responses are similar, demonstrating the representativeness of the obtained finite element model.

It is worth mentioning that only numerical tests were performed by considering the composite hollow shaft under base excitations operating at 992 RPM. Figure 9 shows the vibration responses of the rotor along the x_s and z_s directions of the disks (see Fig. 1). In this case, two simultaneous excitations were applied, i.e., displacement of the rotor base along the x_s and z_s directions, as given by Fig. 9c. The maximum base displacement along the x_s and z_s directions was 0.5 m. The vibration responses obtained at the disks are shown in Fig. 9a and Fig. 9b (full simulation time of 10 s in steps of 0.001s). Note that the vibration responses of the rotor system changed according to the imposed base displacements. As expected, the vibration responses determined along the z_s direction are bigger than the amplitudes obtained along the x_s direction due to the gravity load. The coupling between the vibration responses along the x_s and z_s directions of the rotor is also observed (gyroscopic effect).

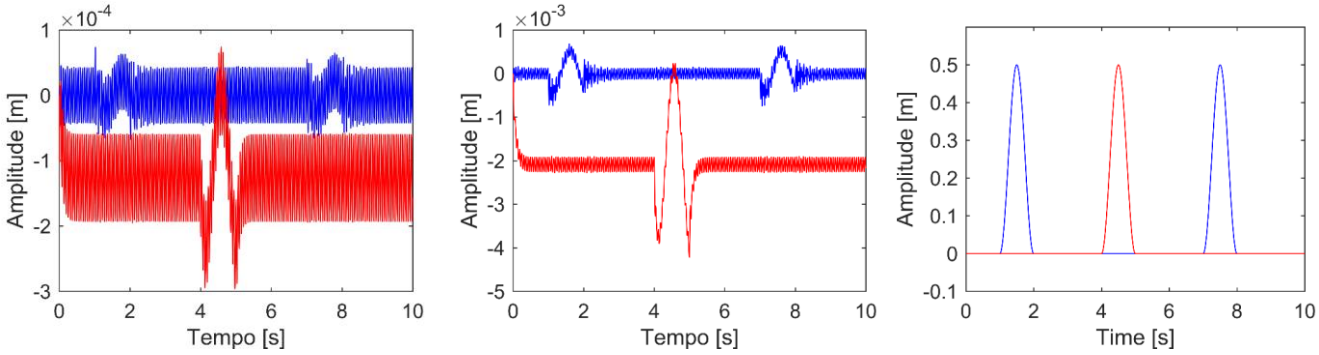

a) vibration responses of disk #1 **b) vibration responses of disk #2** **c) base excitations**

Figure 9 – Vibration responses (---- x_S direction and ---- z_S direction) at the disks of the rotor by considering different base excitations (---- x_0 direction and ---- z_0 direction).

Figures 10a and 10b show the vibration responses of the rotating machine measured along the x_s and z_s directions at the disks D_1 and D_2, respectively (full simulation time of 10 s in steps of 0.001 s). Figure 10c presents the excitation applied to the rotor base which is composed of two angular displacements around the x_s and z_s directions. The maximum base angular displacements around these directions were 0.2 rad. The rotor was operating at 992 RPM. As expected, the vibration responses determined along the x_s and z_s directions changed according to the applied angular displacement. The vibration responses presented in Fig. 10b are bigger then Fig. 10a due to the fact that D_2 is an overhunt disk, presenting amplified dynamic movements. Note that the vibration responses along the x_s and z_s directions of the rotor system are coupled due to the gyroscopic effect.

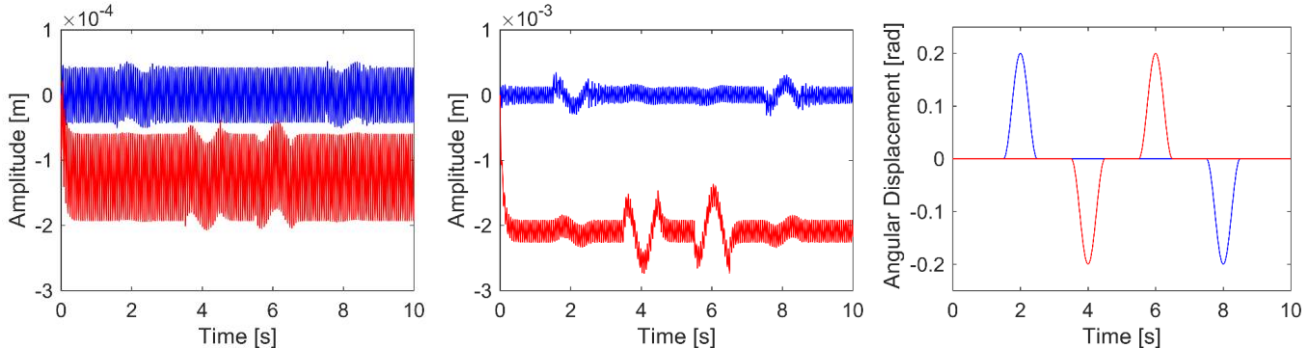

a) vibration responses of disk #1 **b) vibration responses of disk #2** **c) angular displacement**

Figure 10 – Vibration responses (---- x_S direction and ---- z_S direction) determined at disks of the rotor by considering different angular displacements (---- x_0 direction and ---- z_0 direction).

Figure 11 shows the vibration responses of the rotor system along the x_s and z_s directions at the disks D_1 and D_2, respectively (full simulation time of 10 s in steps of 0.001 s) by considering an impact excitation along the x_0 direction combined with a sinusoidal excitation imposed around the z_s direction (Fig. 11c). The sinusoidal excitation is given by:

$$g_s = \mathrm{L}\sin\left(\frac{2p\,\mathrm{W}}{60}t\right) \tag{9}$$

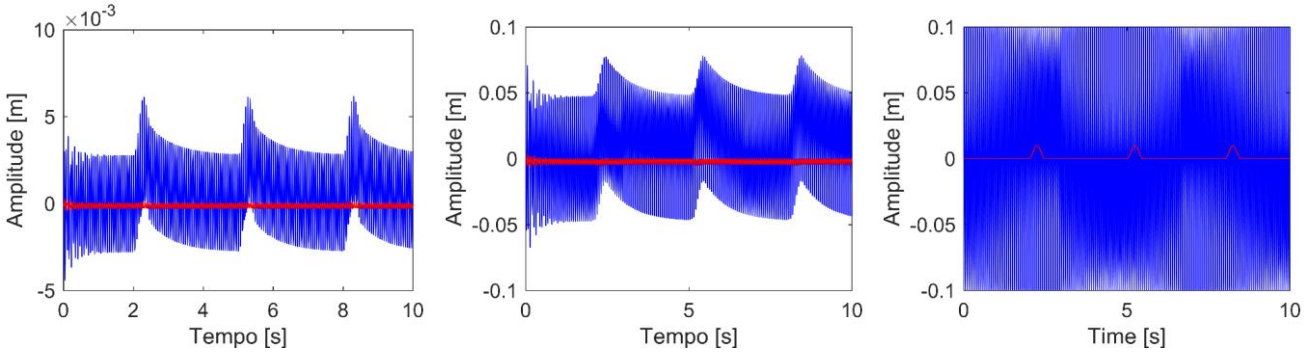

a) vibration responses of disk #1 **b) vibration responses of disk #2** **c) base excitation**

Figure 11 – Vibration responses (---- x_S direction and ---- z_S direction) determined at disks of the rotor by considering combined excitations (---- x_0 direction and ---- z_0 direction); impacts of 0.01 m amplitude.

where Λ was fixed as being equal to 0.1 rad and Ω is the rotation speed of the rotor. In this case, Ω = 992 RPM and a full simulation time of 10 s in steps of 0.001 s were considered. As expected, the combination of two different excitations acting simultaneously in the shaft changed its dynamic behavior. Additionally, even the excitation presenting small amplitudes, the vibration amplitudes of the shaft were bigger than the amplitudes obtained in Figs. 9 and 10.

Figure 12 shows the vibration responses of the rotor determined along the x_s and z_s directions at the disks D_1 and D_2, by considering a sinusoidal excitation applied around the x_s direction as given by:

$$a_s = \mathrm{L}\sin\left(\frac{2p\,\mathrm{W}}{60}t\right) \tag{10}$$

where Λ = 0.1 rad and Ω = 992 RPM (full simulation time of 10 s in steps of 0.001 s). Additionally, an impact excitation was combined with the sinusoidal excitation as presented in Fig. 12c (amplitude bigger than in Fig. 11c; impacts of 0.01 m to 0.1 m amplitude).

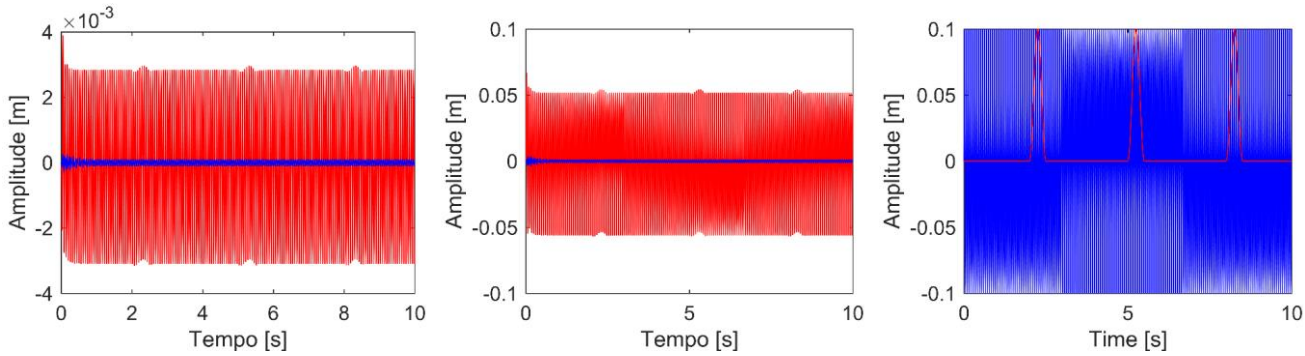

a) vibration responses of disk #1 **b) vibration responses of disk #2** **c) base excitation**

Figure 12 – Vibration responses (---- x_S direction and ---- z_S direction) determined at disks of the rotor by considering combined excitations (---- x_0 direction and ---- z_0 direction); impacts of 0.1 m amplitude.

Note in Figs. 12a and 12b that the vibration responses determined along the z_s direction are bigger than the amplitudes obtained along the x_s direction. This dynamic behavior of the composite shaft is associated with the base excitations, in which a sinusoidal excitation was applied around the x_s direction simultaneously with impacts along the z_0 direction. It is worth mentioning that high excitation amplitudes were used to clearly demonstrate the behavior of the system.

CONCLUSIONS

In the present work, a study on the dynamic behavior of an onboard composite hollow shaft was performed. The vibration responses of the system were obtained both numerically and experimentally. Comparing the numerical and experimental results of Figs. 7 and 8, it was demonstrated that the SHBT formulation can represent the onboard dynamic behavior of the considered composite hollow shaft. Thus, the inherent nonlinearity of the composite shaft presents a small influence on its dynamic behavior. Consequently, the adopted SHBT model (linear model) becomes representative.

In the analyzed base excitations, the vibration responses of the rotor along the z_s direction were more affected than the corresponding responses obtained along the x_s direction. This dynamic behavior is associated with the stiffness of the bearing #2, in which k_{zz} is almost five times smaller than k_{xx} (see Tab. 3). Similarly, the damping coefficient d_{zz} is approximately ten times smaller than d_{xx}.

Thus, the present work sheds new light into some of the phenomena present in onboard and composite dynamics, managing to integrate both effects into the same formulation. Despite having updated the model via experimentation, new and more challenging experiments are being developed. A composite shaft onboard rotor test-rig is currently under design phase and should be tested in the next months, producing new results either to validate the present model or to present new challenges to be understood.

ACKNOWLEDGMENTS

The authors are thankful for the financial support provided to the present research effort by CNPq (574001/2008-5 and 304546/2018-8), FAPEMIG (TEC-APQ-3076-09, TEC-APQ-02284-15, and TEC-APQ-00464-16), and CAPES through the INCT-EIE.

REFERENCES

SILVEIRA, M. E., “Análise do Comportamento Dinâmico de Rotores em Eixos Bobinados”, 2001. 97 p. Masters Thesis, Federal University of Santa Catarina, Florianópolis.

BRUSH, M. “Still Spinning After All These Years: A Profile of The Ultracentrifuge”. The Scientist, v. 13, p. 16-18, Out. 1999.

GUPTA, K. “Composite Shaft Rotor Dynamics: An Overview”. In: Proceedings of VETOMAC, X, 2015, Manchester. Vibration Engineering and Technology of Machinery. p. 79-94.

WETTERGREEN, H.L.; OLSSON, K.O. “Dynamic Instability of a Rotating Asymmetric Shaft with Internal Viscous Damping Supported in Anisotropic Bearings”. Journal of Sound and Vibration, v. 195, p. 75-84, Ago. 1996.

LALANNE, M.; FERRARIS, G. “Rotordynamics Prediction in Engineering”. New York: J. Wiley and Sons, 1998 266p.

SINO, R. “Comportement Dynamique et Stabilite des Rotors: Application aux Rotors Composites”, 2007. 157 p. PhD Thesis, INSA - Lyon, Lyon.

RESPONSIBILITY NOTICE

The authors are the only responsible for the printed material included in this paper.